Journal of Computational Applied Mechanics 2026, 57(3): 473-496

DOI: 10.22059/jcamech.2026.409178.1758

RESEARCH PAPER

Viscoelastic Vibrational and Damping Analysis of Microtubules with Multiple N_S Configurations in Cytosolic Environments

Ali Giv [a], Ali Ghorbanpour Arani [b, *] , Elham Haghparast [c,]

[a] *Ph.D. student Mech. Eng., Faculty of Mechanical Engineering, Kashan University, Kashan*
[b] *Professor, Mech. Eng, Faculty of Mechanical Engineering, Kashan University, Kashan*
[c] *MD student, Medical School. Medical university of Kashan, Kashan*

Abstract

This study investigates the vibrational behavior of anisotropic microtubules (MTs) immersed in the viscous cytosolic fluid using both classical and higher-order beam theories (HOBTs). For the first time, multiple N_S configurations of MTs, along with their precise geometrical characteristics, are analyzed within a novel unified vibration–mechanics framework. The nonlocal strain gradient theory (NSGT) is employed to incorporate size-dependent effects, while surface elasticity theory ensures nanoscale accuracy. Viscoelastic models are integrated for both MTs and their surrounding medium. The intrinsic structural damping of microtubules is examined via the Kelvin–Voigt viscoelastic damping coefficient (retardation time), and the influence of the cytosolic viscous fluid damping on both natural frequencies and damping ratios is thoroughly analyzed. Additional parameters such as the nonlocal parameter, material length scale parameter, microtubule length and various beam theory are also systematically explored. The governing equations and boundary conditions are derived from Hamilton's principle and numerically solved using the Differential Quadrature (DQ) method, enhanced with a CBCGE scheme for efficient boundary implementation. Results reveal that increasing either the structural damping of the MTs or the cytosolic fluid viscosity leads to greater overall damping and a reduction in natural frequencies. A critical retardation time is identified, beyond which the damping ratio rapidly increases, the natural frequencies sharply drop, and the system transitions to a non-oscillatory state. The magnitude of this critical time aligns well with previously reported nanoscale retardation times. The same trend is also observed across different N_S configurations, indicating that smaller microtubules tend to possess higher natural frequencies. These findings highlight the importance of viscoelastic behavior—particularly retardation effects—in understanding cellular mechanics, cancer treatment, disease diagnosis, and bio-nanotechnology advancements.

Keywords: Kelvin–Voigt viscoelastic; Retardation time; Viscoelastic bio-medium; Microtubules N_S configurations; Anisotropic protein microtubules; Higher-order beam theories; nonlocal strain gradient theory; Surface elasticity.

1. Introduction

Microtubules (MTs) are protein-based nanotubular structures that play essential roles in mitosis, intracellular

[*] Corresponding author. *Tel.: +98 31 55912450; Fax: +98 31 55912424.*
E-mail address: aghorban@kashanu.ac.ir; a_ghorbanpour@yahoo.com. (Ali Ghorbanpour Arani)

transport, and cell motility. They exhibit remarkable stiffness (at least one hundred times stiffer than other intracellular components [1]). Experimental investigations [2], using techniques such as phonon spectroscopy, have revealed that MTs possess intrinsic mechanical vibrations in the high-frequency range of hundreds of megahertz to gigahertz.

Unlike most existing vibration–engineering studies [3], which typically model only a single microtubule type (commonly the 13_3 configuration), the present work introduces a more comprehensive novel approach by incorporating multiple N_S configurations of MTs. Although such structural variations have been actively studied in biological and experimental sciences [4], they have not, to the best of the authors' knowledge, been addressed within an analytical or engineering vibration framework with comparable precision.

Another limitation of prior works is the reliance on nominal geometric parameters, in contrast, the current study employs effective dimensions of MTs derived from inter-protofilament bond lengths rather than the nominal tubulin dimer diameters. These refined geometrical values were extracted using data from atomic force microscopy (AFM), electron microscopy, and geometric modeling simulations [5-8], an essential consideration for accurate vibrational analysis, where the results are highly sensitive to such parameters.

This study also introduces a novel and underexplored aspect: the viscoelastic damping behavior of MTs and its surrounding medium. While earlier studies have reported dissipative effects for both the microtubule structure [9] and its surrounding cytosolic medium [10, 11], few have simultaneously examined both contributions in a vibration–mechanics framework. Here, the intrinsic viscoelasticity of MTs is modeled through the Kelvin–Voigt framework, and the associated retardation time is carefully defined and discussed. Additionally, the viscous cytosolic damping effects are incorporated to evaluate their influence on the natural frequencies and damping ratios. Further, the effects of nonlocal parameters, material length-scale parameters, microtubule length and various beam theories (both classical and HOBTs) are systematically analyzed under different N_S configs.

2. Modeling and Kinematics

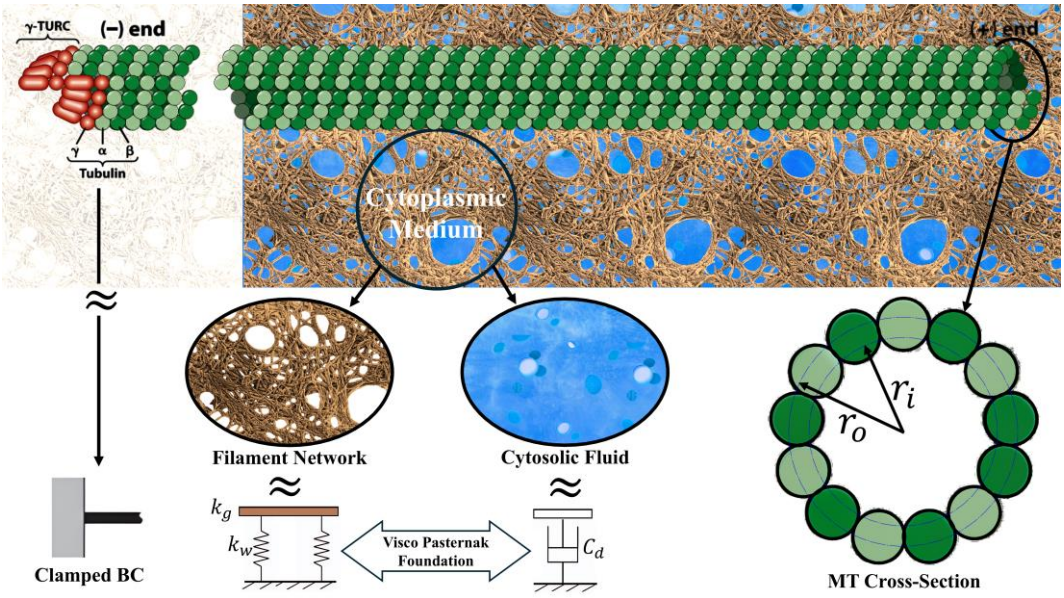

Fig 1: Schematic of a microtubule in the viscoelastic cytoplasmic medium, anchored at its minus end to the (γ-TuRC), as well as effective inner and outer radius of MT.

The cytoplasm, consisting primarily of the cytosol and the filament network, forms a viscoelastic medium that mechanically supports and interacts with microtubules. Because microtubules exhibit a very high slenderness ratio ($L/R \gg 50$), they can be effectively represented by beam-like continuum models. To capture their mechanical response with varying accuracy, several beam formulations are employed and compared, ranging from the Euler–Bernoulli theory (EBT), which neglects transverse shear deformation, to the Timoshenko theory (TBT), which incorporates shear effects through correction factors. In addition, higher-order beam theories (HOBTs) such as the Reddy (RBT), sinusoidal (SBT), hyperbolic (HBT), and exponential (EXBT) models are also considered. These latter formulations include transverse shear deformation without the need for correction factors, as they inherently satisfy the zero shear stress boundary condition at the beam surfaces [12].

Representing MTs as beams also provides an intuitive mechanical analogy for their cellular anchoring conditions. Their minus ends, commonly fixed to the centrosome through the γ-tubulin ring complex (γ-TuRC) [13], correspond to clamped boundaries; their plus ends may be simply supported when linked to the cell cortex via +TIP proteins such as EB1 [13, 14], or free when detached or stabilized by CAMSAP2 [13, 15]. Consequently, a variety of boundary configurations, including clamped–clamped, clamped–free, and simply supported–free, can be found in the cellular environment, reinforcing the suitability of beam theory in describing the mechanical behavior of microtubules.

In this study, a unified higher-order beam theory is employed, encompassing various classical and advanced theories. Within this framework, the axial displacement and the transverse displacement are expressed as the displacement field relations:

$$\begin{aligned} u_1(x,z,t) &= u(x,t) - z\frac{\partial}{\partial x}w(x,t) + f(z)\gamma(x,t) \\ u_2(x,z,t) &= 0 \\ u_3(x,z,t) &= w(x,t) \end{aligned} \tag{1}$$

where u and w denote the axial and transverse displacements of points on the neutral axis, respectively and γ represents the transverse shear strain on the neutral axis:

$$\gamma(x,t) = \frac{\partial}{\partial x}w(x,t) - \varphi(x,t) \tag{2}$$

Here, φ is the total bending rotation of the cross-sections along the neutral axis, and t denotes time. The function f characterizes the transverse shear and stress distribution across the beam's thickness. Different classical and higher-order beam theories can be recovered by appropriately selecting $f(z)$, as follows:

$$\begin{aligned} &\text{EBT: } f(z) = 0 \\ &\text{TBT: } f(z) = z \\ &\text{RBT: } f(z) = z\left(1 - \frac{z^2}{3\,r_o^{\,2}}\right) \\ &\text{SBT: } f(z) = \frac{2\,r_o}{\pi}\,sin\left(\frac{\pi z}{2\,r_o}\right) \\ &\text{HBT: } f(z) = 2\,r_o\,\,sinh\left(\frac{z}{2\,r_o}\right) - z\,cosh\left(\frac{1}{2}\right) \\ &\text{EXBT: } f(z) = ze^{-2\left(\frac{z}{2\,r_o}\right)^2} \end{aligned} \tag{3}$$

By differentiating the displacement fields, the strain–displacement relations are obtained as:

$$\begin{aligned} \varepsilon_{xx} &= \frac{\partial}{\partial x}u(x,t) - f(z)\frac{\partial}{\partial x}\varphi(x,t) - \left(z - f(z)\right)\frac{\partial^2}{\partial x^2}w(x,t) \\ \gamma_{xz} &= \left(\frac{\mathrm{d}}{\mathrm{d}z}f(z)\right)\left(\frac{\partial}{\partial x}w(x,t) - \varphi(x,t)\right) \\ \varepsilon_{yy} &= \varepsilon_{zz} = \gamma_{xy} = \gamma_{yz} = 0 \end{aligned} \tag{4}$$

3. System energies

3.1. The strain energy

The governing equations and boundary conditions are derived using the energy method, which involves

calculating various system energies and applying Hamilton's principle. The variation of the strain energy of MT (δU) is defined as:

$$\begin{aligned}
&\delta U = \int_V \sigma_{ij}\delta\varepsilon_{ij}dV \rightarrow \delta U = \int_V \sigma_{xx}\delta\varepsilon_{xx} + \tau_{xz}\delta\gamma_{xz}dV \\
&\delta U = \int_A \int_0^L \sigma_{xx}\delta\left(\frac{\partial}{\partial x}u(x,t) - f(z)\frac{\partial}{\partial x}\varphi(x,t) - (z-f(z))\frac{\partial^2}{\partial x^2}w(x,t)\right) \\
&+\tau_{xz}\delta\left(\left(\frac{\mathrm{d}}{\mathrm{d}z}f(z)\right)\left(\frac{\partial}{\partial x}w(x,t) - \varphi(x,t)\right)\right)dxdA
\end{aligned} \tag{5}$$

Where L is the length of the microtubule and the following stress resultants are defined as:

$$\begin{aligned}
&N(x,t) = \int_A \sigma_{xx}dA \\
&M(x,t) = \int_A \sigma_{xx}zdA \\
&M_n(x,t) = \int_A \sigma_{xx}f(z)dA \\
&Q(x,t) = \int_A \tau_{xz}\left(\frac{\mathrm{d}}{\mathrm{d}z}f(z)\right)dA
\end{aligned} \tag{6}$$

Finally, applying the variation operator δ to the strain energy function yields a portion of the governing equations along with the corresponding boundary conditions:

$$\begin{aligned}
&\delta U = \int_0^L -\left(\frac{\partial}{\partial x}N(x,t)\right)\delta u(x,t) + \left(\frac{\partial}{\partial x}M_n(x,t)\right)\delta\varphi(x,t) - \left(\frac{\partial^2}{\partial x^2}M(x,t)\right)\delta w(x,t) \\
&+\left(\frac{\partial^2}{\partial x^2}M_n(x,t)\right)\delta w(x,t) - \left(\frac{\partial}{\partial x}Q(x,t)\right)\delta w(x,t) - Q(x,t)\delta\varphi(x,t)dx \\
&+ \\
&N(x,t)\delta u(x,t)\Big|_0^L - M_n(x,t)\delta\varphi(x,t)\Big|_0^L - M(x,t)\left(\frac{\partial}{\partial x}\delta w(x,t)\right)\Big|_0^L + \left(\frac{\partial}{\partial x}M(x,t)\right)\delta w(x,t)\Big|_0^L \\
&+M_n(x,t)\left(\frac{\partial}{\partial x}\delta w(x,t)\right)\Big|_0^L - \left(\frac{\partial}{\partial x}M_n(x,t)\right)\delta w(x,t)\Big|_0^L + Q(x,t)\delta w(x,t)\Big|_0^L
\end{aligned} \tag{7}$$

3.2. The kinetic energy

The general expression for the kinetic energy of the microtubule is given as:

$$K = \frac{1}{2}\rho\int_V \left(\frac{\partial}{\partial t}u_1(x,z,t)\right)^2 + \left(\frac{\partial}{\partial t}u_2(x,z,t)\right)^2 + \left(\frac{\partial}{\partial t}u_3(x,z,t)\right)^2 dV \tag{8}$$

Where ρ is the mass density of MT. By substituting the displacement field relations (1) into the kinetic energy expression, the expanded form of the kinetic energy is obtained as follows:

$$
\begin{aligned}
K = \frac{1}{2}\rho\int_0^L & -2I_3\left(\frac{\partial^2}{\partial x\partial t}w(x,t)\right)^2 + 2I_3\left(\frac{\partial^2}{\partial x\partial t}w(x,t)\right)\left(\frac{\partial}{\partial t}\varphi(x,t)\right) + I_1\left(\frac{\partial^2}{\partial x\partial t}w(x,t)\right)^2 \\
& + I_4\left(\frac{\partial^2}{\partial x\partial t}w(x,t)\right)^2 + 2I_2\left(\frac{\partial^2}{\partial x\partial t}w(x,t)\right)\left(\frac{\partial}{\partial t}u(x,t)\right) - 2I_4\left(\frac{\partial^2}{\partial x\partial t}w(x,t)\right)\left(\frac{\partial}{\partial t}\varphi(x,t)\right) \\
& - 2I_2\left(\frac{\partial}{\partial t}\varphi(x,t)\right)\left(\frac{\partial}{\partial t}u(x,t)\right) + I_4\left(\frac{\partial}{\partial t}\varphi(x,t)\right)^2 + A\left(\frac{\partial}{\partial t}u(x,t)\right)^2 + A\left(\frac{\partial}{\partial t}w(x,t)\right)^2 \\
& - 2I_0\left(\frac{\partial}{\partial t}u(x,t)\right)\left(\frac{\partial^2}{\partial x\partial t}w(x,t)\right)dx
\end{aligned}
\tag{9}
$$

Where the cross-sectional higher-order moments are defined as:

$$
\begin{aligned}
I_0 &= \int_A z dA = 0 \\
I_1 &= \int_A z^2 dA \\
I_2 &= \int_A f(z) dA = 0 \\
I_3 &= \int_A f(z).z dA \\
I_4 &= \int_A f(z)^2 dA
\end{aligned}
\tag{10}
$$

Since both the functions $f(z)$ and z are odd, the two moments above I_0 and I_2 will always evaluate to zero when integrated over the symmetric domain of the cross-section. By applying the first variation to the kinetic energy relation (9), another portion of governing equations, along with the corresponding boundary conditions, is derived:

$$
\begin{aligned}
\int_0^T \delta K dt = \int_0^T\int_0^L & \left(\begin{array}{l}
\rho(-2I_3 + I_1 + I_4)\left(\frac{\partial^4}{\partial x^2\partial t^2}w(x,t)\right)\delta w(x,t) + \rho(I_3 - I_4)\left(\frac{\partial^3}{\partial x\partial t^2}\varphi(x,t)\right)\delta w(x,t) \\
-\rho(I_3 - I_4)\left(\frac{\partial^3}{\partial x\partial t^2}w(x,t)\right)\delta\varphi(x,t) - \rho I_4\left(\frac{\partial^2}{\partial t^2}\varphi(x,t)\right)\delta\varphi(x,t) \\
-\rho A\left(\frac{\partial^2}{\partial t^2}u(x,t)\right)\delta u(x,t) - \rho A\left(\frac{\partial^2}{\partial t^2}w(x,t)\right)\delta w(x,t)
\end{array}\right) dx dt \\
& + \\
& \rho(-2I_3 + I_1 + I_4)\int_0^L\left(\frac{\partial^2}{\partial x\partial t}w(x,t)\right)\cancel{\left(\frac{\partial}{\partial x}\delta w(x,t)\right)}dx\Bigg|_0^T - \rho(-2I_3 + I_1 + I_4)\int_0^T\left(\frac{\partial^3}{\partial x\partial t^2}w(x,t)\right)\delta w(x,t)dt\Bigg|_0^L \\
& + \rho(I_3 - I_4)\int_0^L\left(\frac{\partial}{\partial t}\varphi(x,t)\right)\cancel{\left(\frac{\partial}{\partial x}\delta w(x,t)\right)}dx\Bigg|_0^T - \rho(I_3 - I_4)\int_0^T\left(\frac{\partial^2}{\partial t^2}\varphi(x,t)\right)\delta w(x,t)dt\Bigg|_0^L \\
& + \rho(I_3 - I_4)\int_0^L\left(\frac{\partial^2}{\partial x\partial t}w(x,t)\right)\cancel{\delta\varphi(x,t)}dx\Bigg|_0^T + \rho I_4\int_0^L\left(\frac{\partial}{\partial t}\varphi(x,t)\right)\cancel{\delta\varphi(x,t)}dx\Bigg|_0^T \\
& + \rho A\int_0^L\left(\frac{\partial}{\partial t}u(x,t)\right)\cancel{\delta u(x,t)}dx\Bigg|_0^T + \rho A\int_0^L\left(\frac{\partial}{\partial t}w(x,t)\right)\cancel{\delta w(x,t)}dx\Bigg|_0^T
\end{aligned}
\tag{11}
$$

3.3. Elastic Medium Energy and the Visco-Pasternak Model

Microtubules are embedded in the cytoplasm (cytoskeletal MTs) or axoplasm (axonal MTs). These surrounding viscoelastic media are modeled using a Visco-Pasternak foundation, where the total force is decomposed into an elastic (Pasternak) and a viscous component. The work of each component is computed separately and incorporated into Hamilton's principle. The total surrounding medium force is expressed as:

$$p_{visco-elastic\ media} = p_1 + p_2 \tag{12}$$

Where:

$$\begin{aligned} p_1 &= k_w w - k_g \nabla^2 w \\ p_2 &= -C_d \dot{w} \end{aligned} \tag{13}$$

Here, p_1 is the conservative Pasternak (elastic) force, while p_2 is the non-conservative, velocity-dependent viscous force. Accordingly, p_1 contributes through potential energy, whereas p_2 enters via its external work term in Hamilton's principle. The negative sign of p_2 indicates its opposition to motion and energy dissipation. The potential energy of the elastic foundation due to p_1 is given by:

$$V = \frac{1}{2}\int_0^L \left(k_w w - k_g \nabla^2 w\right) w\, dx \tag{14}$$

Where ∇^2 denotes the Laplacian operator, which, under beam theory assumptions, reduces to $\nabla^2 = \partial^2 / \partial x^2$. Thus, the total potential energy of the elastic medium, can be obtained as:

$$V = \frac{1}{2}\int_0^L \left(k_w \left(w(x,t)\right)^2 - k_g w(x,t)\left(\frac{\partial^2}{\partial x^2} w(x,t)\right)\right) dx \tag{15}$$

And its variational form:

$$\begin{aligned} \delta V = &\int_0^L \left(k_w w(x,t) - k_g \left(\frac{\partial^2}{\partial x^2} w(x,t)\right)\right) \delta w(x,t)\, dx \\ &+ \\ &-\frac{1}{2} k_g w(x,t)\left(\frac{\partial}{\partial x}\delta w(x,t)\right)\Big|_0^L + \frac{1}{2} k_g \left(\frac{\partial}{\partial x} w(x,t)\right)\delta w(x,t)\Big|_0^L \end{aligned} \tag{16}$$

In contrast, p_2 is a non-conservative viscous force and cannot be expressed as potential energy and then taken the variation. Instead, its variational form must be considered directly, adding the term $\int_0^T \delta W_{nc} dt$ to Hamilton's principle:

$$\delta \int_0^T (K - \Pi + W_E)\, dt + \int_0^T \delta W_{nc} dt = 0 \tag{17}$$

Whereas the versional form of the work of the viscous force is as follows:

$$\delta W_{nc} = \int_0^L - C_d \dot{w} \delta w \tag{18}$$

The coefficients k_w , k_g , and C_d associated with the Visco-Pasternak model are determined from the mechanical properties of the surrounding filamentous network and cytosolic fluid:

k_w is the spring stiffness (Winkler constant) of the filament network and, based on Teng Li's research [16], is given by $k_w = 2.7E_c$, where E_c is the network elastic modulus. The Pasternak shear modulus k_g is typically expressed as a fraction of k_w , such that the dimensionless shear modulus is approximately one-tenth of the dimensionless spring stiffness [3, 17]:

$$\frac{k_g}{E \cdot A} = C_g \cdot \frac{k_w}{E}, \qquad C_g \approx 0.1 \tag{19}$$

The damping coefficient C_d , representing the cytosolic viscous effect, is obtained by integrating the viscous stress at the microtubule/cytoplasm interface:

$$C_d = \pi \mu_c \eta \tag{20}$$

Where μ_c is the dynamic viscosity of the cytosol and η is defined by:

$$\eta = \frac{\left((1-q^4)\ln(q) - 12q^2 + 2q^4 + 10\right)}{\left((q^4-1)\ln(q) + 2q^2 - q^4 - 1\right)}, \qquad q = \frac{r_o}{R_1} \tag{21}$$

Here, r_o is the outer radius of the microtubule, and R_1 is the radial distance from the microtubule centerline at which the induced viscous flow vanishes. The derivation of C_d is based on the Navier–Stokes equations for Newtonian fluid motion, the definition of cytosolic viscous stress, and the continuity condition for incompressible fluid. Boundary conditions include the no-slip condition at the microtubule–cytosol interface (equality of wall and fluid velocities) and a far-field condition where fluid velocity is assumed to be zero at a specified distance R_1 from the microtubule [16].

4. Governing equations

4.1. Classical governing equations

Hamilton's principle for this system can be expressed as follows:

$$\delta \int_0^T \left(K - (U+V) + W_E\right) dt + \int_0^T \delta W_{nc} dt = 0 \tag{22}$$

It is also possible to move the variation operator δ inside the integral, yielding the following expression:

$$\int_0^T \delta L \, dt + \int_0^T \delta W_{nc} dt = \int_0^T \left(\delta K - \delta U - \delta V + \delta W_E + \delta W_{nc}\right) dt = 0 \tag{23}$$

By applying Hamilton's principle and setting the coefficients of δu , δw , and $\delta \varphi$ to zero, the classical governing equations or classical equations of motion of the system are obtained.

4.2. Surface Elasticity Theory

According to Gurtin–Murdoch surface elasticity theory [18], the surface layer (conceptualized as a single-atom-thick layer at the outer boundaries of materials) induces additional stress fields. While negligible at macroscopic scales, these stresses become significant at micro- and nanoscale dimensions. This theory introduces two fundamental sets of key relations:

1. **Surface Constitutive Relations** – describing surface layer elasticity independently.

$$\sigma_{xx}^{s} = E^{s}\varepsilon_{xx} + \tau^{s}, \qquad \tau_{xz}^{s} = \tau^{s}\left(\frac{\partial}{\partial x}w(x,t)\right) \tag{24}$$

Where E^s and τ^s are the surface Young's modulus and the residual surface tension respectively.

2. **Bending-Induced Relation** – accounting for residual surface tension (τ^s) effects, exclusively during bending.

$$\sigma_{zz} = f^{s}(z)\left(\tau^{s}\frac{\partial^2 w}{\partial x^2} - \rho^{s}\frac{\partial^2 w}{\partial t^2}\right) \tag{25}$$

Relation (25) derived after successive simplifications [18] from the surface layer's dynamic equilibrium including both bulk and surface stresses, where ρ^s is the surface density. The stress distribution function $f^s(z)$ reaches extremum values at the surface boundaries and varies linearly through the bulk thickness.

4.3. Constitutive relations of orthotropic MT

To determine the most accurate constitutive relation (plane stress or plane strain) for such a beam (considering the surface-to-bulk stress σ_{zz}) the displacement field must be considered, in which $\varepsilon_{yy} = \gamma_{xy} = \gamma_{yz} = 0$. These conditions explicitly confirm the validity of the **plane strain** assumption, which is therefore adopted. By neglecting y-direction strains in the general stress–strain relation for an orthotropic material, inverting the relation, and using compliance matrix symmetry, finally the constitutive relation for the orthotropic beam under plane strain condition is obtained:

$$\sigma_{xx} = \frac{E_x^*}{1-\nu_{xy}\nu_{yx}}\varepsilon_{xx} + \frac{\nu_{xy}\nu_{yz}+\nu_{xz}}{1-\nu_{xy}\nu_{yx}}\sigma_{zz} \tag{26}$$

Here, the value of ν_x reported in the Bio articles will be used for the ν_{xy} and ν_{xz}. Also, the value of ν_θ, which we had from the symmetry of the compliance matrix as $\nu_\theta = \nu_x\frac{E_\theta}{E_x}$, will be used for ν_{yz} and ν_{yx}, [19]. Also, constitutive relation for shear stress will be as follows:

$$\tau_{xz} = \kappa G_{xz}^{*}\gamma_{xz} \tag{27}$$

Here, κ represents the shear correction factor of the bulk zone, and E^* and G^* denote the Young's modulus and shear modulus of the viscoelastic MT, respectively. EBT ignores transverse shear strain by assuming plane cross-sections remain perpendicular to the beam axis after deformation, resulting in zero shear correction factor, $\kappa = 0$. In contrast, TBT allows cross-sections to rotate, accounting for transverse shear strain and requiring a non-zero shear correction factor $\kappa \neq 0$, which depends on the cross-section geometry. In most references, the shear correction factor for a rectangular cross-section is taken as $\kappa = 5/6 = 0.833$. This value is derived based on the following equation [20], but for thick-walled hollow circular cross-sections (annulus), the shear correction factor is given by [20]:

Table 1: Shear correction factor, κ for TBT

Rectangular cross-section	Thin-walled hollow circular cross-sections	Thick-walled hollow circular cross-sections
$\kappa = \frac{10.(1+\nu)}{12+11\nu}$	$\kappa = \frac{2.(1+\nu)}{4+3\nu}$	$\kappa = \frac{6.(1+\nu).(1+m^2)^2}{(7+6\nu).(1+m^2)^2+(20+12\nu).m^2}$ (28)

Where ν is Poisson's ratio and $m = r_i / r_o$ is the ratio of inner to outer radii. To calculate the shear correction factor in TBT, the mechanically effective inner and outer radius and wall thickness each MT configuration—derived from inter-protofilament bond lengths rather than the nominal geometric diameter of tubulin dimers—are used from Table 2, [4-6]:

Table 2: Inner and outer radius, thickness, aspect ratio, shear correction factor (TBT) for different configs

N_S configs	r_i	r_o	thickness h	h/r	κ (thick-walled)
10_2	6.9	9.65	2.75	0.285	0.554
12_2	8.64	11.4	2.76	0.242	0.547
12_3	8.81	11.54	2.73	0.237	0.546
13_3	9.32	12.11	2.79	0.230	0.545
14_2	9.97	12.8	2.83	0.221	0.544
14_3	10.19	12.98	2.79	0.215	0.543
14_4	9.94	12.77	2.83	0.222	0.544
15_3	10.78	13.62	2.84	0.209	0.542

As can be seen, these values yield an thickness-to-radius ratio of about $h/r \approx 0.2$ or highr, classifying the MT as a thick-walled hollow circular cross-section (typically, the ratios $h/r > 0.1$ are considered thick-walled). Substituting these parameters into relation (28) yields the shear correction factor of the TBT. The values obtained are listed in Table 2 for each individual MT N–S configuration and are generally around 0.54, these values were calculated based on the thick-walled hollow circular cross-section formulation, whereas using the thin-walled formulation yields an identical value of 0.531 for all configurations.

Higher-order beam theories (HOBTs), which incorporate cross-sectional warping, satisfy the zero transverse shear stress boundary conditions on the upper and lower surfaces of the beam and therefore do not require a shear correction factor; accordingly, $\kappa = 1$ is typically assumed.

Also E^* and G^* can be derived based on the Kelvin–Voigt viscoelastic model as follows:

$$E_x^* = E_x\left(1 + g\frac{\partial}{\partial t}\right), \qquad G_{xz}^* = G_{xz}\left(1 + g\frac{\partial}{\partial t}\right) \tag{29}$$

Where g is Retardation time of MT in Kelvin–Voigt viscoelastic damping model which is introduced and discussed in detail in the next section.

4.4. Structural Viscoelasticity of Microtubules

Microtubules exhibit viscoelastic behavior due to their protein structure. In modeling their intrinsic structural viscoelasticity, the Kelvin–Voigt model is employed, which represents the material as a spring (elastic modulus E) and a dashpot (dynamic viscosity η) connected in parallel **Error! Reference source not found.**(a). The constitutive relation can be expressed as:

$$\sigma = E\left(1 + g\frac{\partial}{\partial t}\right)\varepsilon \tag{30}$$

Or equivalently as $\sigma = E\varepsilon + \eta\dot{\varepsilon}$, where $g = \eta/E$ represents the ratio of viscosity to stiffness and has the dimension of time. In the Kelvin–Voigt model, this characteristic time is referred to as the "retardation time", which quantifies the delay in strain response under a constant applied stress. In contrast, in the Maxwell model, **Error! Reference source not found.**(b), the same quantity $\tau = \eta/E$ is called the "relaxation time", describing the stress decay under constant strain.

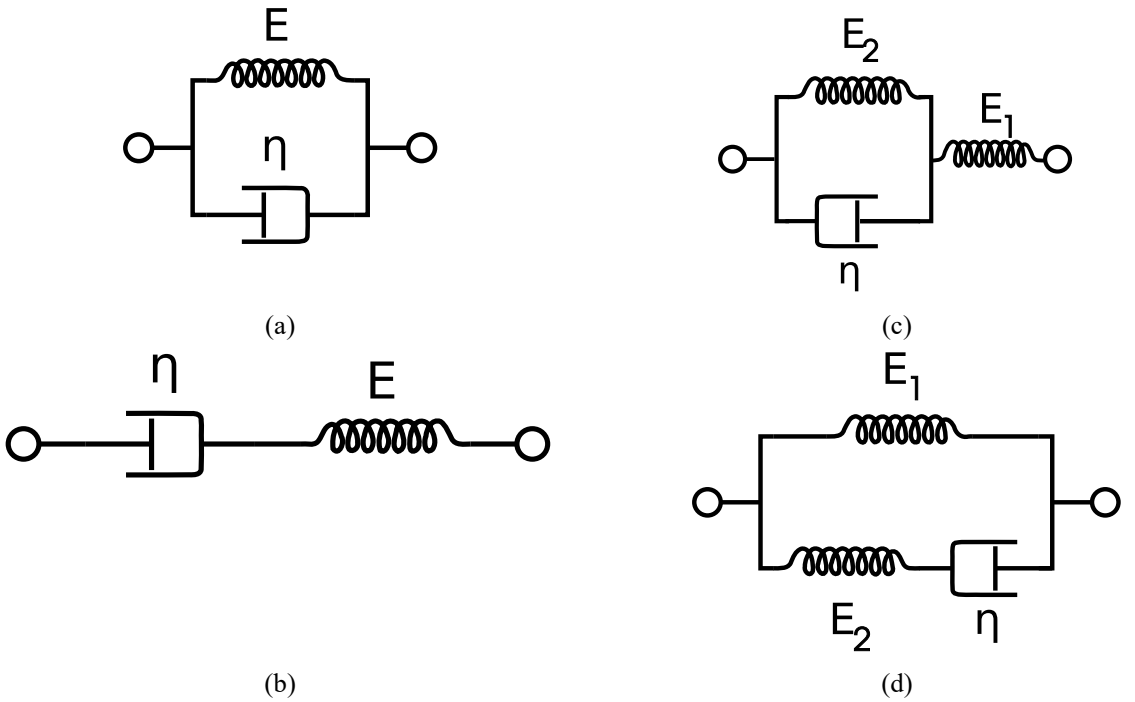

Fig 2: Schematic diagram of viscoelastic (a) Kelvin–Voigt model, (b) Maxwell model, (c) SLS model (Kelvin representation), (d) SLS model (Maxwell representation).

In the Kelvin–Voigt model, a larger g indicates a more viscous, time-dependent response (as an example, polymeric materials with their relatively high viscosity, typically exhibit a longer retardation time (g), meaning they deform gradually and with a delay after the application of stress). In contrast a smaller g corresponds to a stiffer, more elastic response (as an example of materials with a small g , metallic materials can be mentioned, where the retardation time is typically shorter because elastic behavior dominates, and metals respond more quickly to applied loads).

Physically, the retardation time characterizes the time required for the system to reach a new equilibrium after deformation, describing how energy dissipates through internal damping. If the loading duration is much shorter than g , the microtubule behaves elastically; if it is much longer, it exhibits gradual, viscous deformation.

Various analytical and experimental studies indicate that this characteristic time is in the order of nanoseconds. Using the non-destructive experimental method of the oscillating rod rheometer (ORR) [21], the dynamic viscosity of microtubules was reported in the range of 1.5 – 124 mPa·s. Given the elastic modulus of MT ($E = 1.1 Gpa$), the retardation time ($g = \eta / E$) can be estimated, resulting in values on the order of tens of nanoseconds or smaller.

In another approach, several analytical studies [22-24] estimated the relaxation time (τ) by dividing the average kinetic energy stored in a microtubule by the rate of energy dissipation per unit length, yielding $\tau \approx 0.26\,\text{ns}$.

In a third approach, some studies [25] have modeled the viscoelasticity of microtubules using the Standard Linear Solid (SLS) model (**Error! Reference source not found.**(c,d), a Zener-type combination of Kelvin–Voigt and Maxwell elements) for computational simulations. These studies also clearly indicate that the characteristic retardation time for microtubules lies in the "nanosecond range".

4.5. Nonlocal strain gradient theory (NSGT)

At the nanoscale, classical continuum models lose validity due to size-dependent effects. To address this, Eringen's nonlocal elasticity and the strain gradient theory introduce the nonlocal parameter $\mu = e_0 a$ and the material length scale l , respectively. Their combination forms the Nonlocal Strain Gradient Theory (NSGT) [26], used in this study. The constitutive relation of NSGT couples nonlocal and gradient effects as:

$$\left(1 - \mu^2 \nabla^2\right) t_{xx} = E\left(1 - l^2 \nabla^2\right) \varepsilon_{xx} \tag{31}$$

Or equivalently, using classical stress σ_{ij}^{cl} :

$$\left(1-\mu^2\nabla^2\right)t_{ij}=\left(1-l^2\nabla^2\right)\sigma_{ij}^{cl} \tag{32}$$

Integrating over the cross-sectional area A and surface boundaries Γ_1 and Γ_2 yields the stress resultants:

$$\left(1-\mu^2\nabla^2\right)\{N,M,M_n,Q\}^{ncl}=\left(1-l^2\nabla^2\right)\{N,M,M_n,Q\}^{cl} \tag{33}$$

Substituting these relations into the classical beam equations using a specific multi-step substitution technique provides the non-classical governing equations of the microtubule within the NSGT–surface elasticity framework. The corresponding relations for the classical and non-classical stress resultants are listed in the Appendix.

5. Solution method

The governing equations are solved using the Differential Quadrature (DQ) method, known for its high accuracy and fast convergence. The response functions are first separated into spatial and temporal parts as:

$$W(X,\tau)=\overline{W}(X)e^{\hat{\omega}\tau},\quad \phi(X,\tau)=\bar{\phi}(X)e^{\hat{\omega}\tau} \tag{34}$$

Where $\hat{\omega}=\omega\cdot L\cdot\sqrt{\dfrac{\rho}{E}}$ is the dimensionless complex natural frequency and ω is the complex. In the DQ method, spatial derivatives at discrete grid points are approximated by weighted sums of function values at all nodes:

$$\frac{\partial^n}{\partial X^n}(\bar{W}_i,\bar{\phi}_i)=\sum_{j=1}^{N}A_{ij}^{(n)}(\bar{W}_j,\bar{\phi}_j),\quad i=1,\ldots,N \tag{35}$$

Here, $A_{ij}^{(n)}$ denotes the weighting coefficient matrix of n-order of the (DQ) method. The first-order coefficient matrix of the DQ is defined as:

$$A_{ij}^{(1)}=\begin{cases}for\, i\neq j\rightarrow A_{ij}^{(1)}=\dfrac{\prod\limits_{\substack{k=1\\k\neq i,j}}^{N}(x_i-x_k)}{\prod\limits_{\substack{k=1\\k\neq j}}^{N}(x_j-x_k)} & i,j=1,2,...,N\\ for\, i=j\rightarrow A_{ij}^{(1)}=\sum\limits_{k=1,k\neq i}^{N}\dfrac{1}{x_i-x_k} & i=1,2,...,N\end{cases} \tag{36}$$

Where these weighting coefficients matrices are determined from Chebyshev grid points:

$$x_i=\underbrace{\frac{1}{2}\left(1-\cos\left(\frac{\pi(i-1)}{N-1}\right)\right)}_{Chebyshev\ points},\quad i=1,\ldots,N \tag{37}$$

Higher-order weighting matrices are obtained recursively from the first-order matrix $\left[A^{(n)}\right]=\left[A^{(1)}\right]\left[A^{(n-1)}\right]$. Applying DQ discretization converts the governing differential equations into an algebraic eigenvalue system:

$$\begin{aligned}&\delta W,\delta\phi:\\&\hat{\omega}^2\left[M\right]_{2N\times 2N}\left\{\bar{d}\right\}_{2N}+\hat{\omega}\left[C\right]_{2N\times 2N}\left\{\bar{d}\right\}_{2N}+\left[K\right]_{2N\times 2N}\left\{\bar{d}\right\}_{2N}=0\end{aligned} \tag{38}$$

Where $\{\bar{d}\}$ is the displacement vector $\{\bar{d}\}=\left\{\{\overline{W}_1,\overline{W}_2,\ldots,\overline{W}_N\},\{\bar{\phi}_1,\bar{\phi}_2,\ldots,\bar{\phi}_N\}\right\}^T$.

5.1. Implementing of boundary conditions

A similar discretization procedure is applied to the boundary conditions. As a result, two systems of equations are obtained: one corresponding to the discretized governing equations (38), and another associated with the discretized boundary conditions. When these two systems are examined simultaneously, a fundamental issue arises at the boundary nodes. Specifically, multiple equations may be associated with a single boundary node, including one governing equation together with one or more boundary condition equations (e.g., Dirichlet-type displacement constraints and derivative-type boundary conditions). Since a unique solution must be assigned to each unknown, the coexistence of multiple equations at a single node is not permissible.

It should be noted that, at boundary nodes, the governing equations must be discarded because the solution at these nodes is governed exclusively by the prescribed boundary conditions. However, even after removing the governing equations, the issue may persist if multiple boundary conditions are imposed at the same boundary node. To address this issue and to ensure a proper and consistent implementation of boundary conditions within the differential quadrature framework, three well-established techniques have been proposed in the literature: (i) the δ-technique [27], (ii) the modification of weighting coefficient matrices [27], and (iii) the direct substitution of boundary conditions into the discretized governing equations [27].

In this study, boundary conditions are imposed using the third approach, referred to as the coupled boundary condition and governing equation (CBCGE) method. To implement the CBCGE approach, the system is partitioned into two parts: the interior points or domain d ($3\le i\le N-2$) and the boundary points b ($i=1,2,N-1,N$) (for EBT). This separation is initially applied to the displacement vector through a reordering process in which all boundary degrees of freedom are grouped together, followed by the interior degrees of freedom until finally the displacement vector takes the form $\{\bar{d}\}=\begin{Bmatrix}\{\bar{d}_b\}\\ \{\bar{d}_d\}\end{Bmatrix}$.

Consistently, the same permutation is applied to the global stiffness, damping, and mass matrices. Specifically, the columns associated with boundary nodes are rearranged to precede those corresponding to interior nodes, ensuring that the algebraic structure of the governing equations remains unchanged. Subsequently, the rows of these matrices are reordered in the same manner, such that the boundary-related rows appear at the top and the interior rows at the bottom. Therefore, without any change in the algebraic and mathematical structure of the governing equations, it can be rearranged as follows:

$$\hat{\omega}^2\begin{bmatrix}[M_{bb}] & [M_{bd}]\\ [M_{db}] & [M_{dd}]\end{bmatrix}\begin{Bmatrix}\{\bar{d}_b\}\\ \{\bar{d}_d\}\end{Bmatrix}+\hat{\omega}\begin{bmatrix}[C_{bb}] & [C_{bd}]\\ [C_{db}] & [C_{dd}]\end{bmatrix}\begin{Bmatrix}\{\bar{d}_b\}\\ \{\bar{d}_d\}\end{Bmatrix}+\begin{bmatrix}[K_{bb}] & [K_{bd}]\\ [K_{db}] & [K_{dd}]\end{bmatrix}\begin{Bmatrix}\{\bar{d}_b\}\\ \{\bar{d}_d\}\end{Bmatrix}=0 \tag{39}$$

By perform a similar separation on the boundary condition equations $[T]\{\bar{d}\}=0$, we will have it in the separated form $[T_b]\{\bar{d}_b\}+[T_d]\{\bar{d}_d\}=0$ and finally, by substituting column vector $\{\bar{d}_b\}=-[T_b]^{-1}[T_d]\{\bar{d}_d\}$ into the main system (39), an equivalent reduced eigenvalue problem is obtained:

$$\hat{\omega}^2[M_f]\{\bar{d}_d\}+\hat{\omega}[C_f]\{\bar{d}_d\}+[K_f]\{\bar{d}_d\}=0 \tag{40}$$

The matrix dimensions depend on the beam theory used $(N-4)\times(N-4)$ for EBT, $(2N-4)\times(2N-4)$ for TBT, and $(2N-6)\times(2N-6)$ for HOBTs. The resulting quadratic eigenvalue problem (QEP) yields the system's dimensionless complex natural frequencies $\hat{\omega}$.

6. Validation and verification

To validate the accuracy of the developed formulations, the selected numerical scheme, and the implemented computational algorithm, identical physical and material parameters to those reported in previous studies were utilized. The resulting comparisons exhibit a remarkable level of agreement with the published reference data, thereby verifying the consistency, precision, and reliability of the present modeling approach (see Table 3).

Table 3: First two natural frequencies of the microtubule (MHZ)

($theory = EBT,\ BC = SS,\ r_o = 14.05nm,\ r_i = 11.35nm,\ L = 2\mu m,\ \rho = 1470kg/m^3,\ E = 2Gpa,\ \nu = 0.3$)

Mode	Gu et al, 2009 [28] (analytical)*	Civaleket et al, 2010 [29] (DQM, N=11)	A G Arani et al, 2015 [19] (analytical)	Present work (DQM, N=11)
1	25.993	25.968	26.040	25.991
2	103.972	103.962	104.200	103.857

In addition to the above analytical validations, experimental confirmation can be found in the literature. The present study predicts natural frequencies of microtubule vibrations in the range of hundreds of megahertz. This frequency scale is consistent with experimental observations reported by Aslam and Prodan [2], who experimentally measured the phonon spectrum of microtubules by analyzing transverse collective vibrational modes induced by thermal fluctuations. The experimentally reported MHz-range phonon frequencies provide strong support for the relevance of the frequency domain predicted in the present analytical work.

To further strengthen the validation of the present analytical model, a direct comparison with available experimental data has been performed. The experimentally measured phonon spectrum of microtubules reported by Aslam and Prodan [2] was considered as a benchmark. In particular, the microtubule with a length of 8.9 μm and a flexural rigidity of 6×10^{-24} N·m² (as listed in Table 1 of the reference [2]) was selected, and the same parameters were implemented in the present numerical model. Using these experimentally reported mechanical properties, the predicted fundamental frequency obtained from the current formulation falls within the MHz regime, with a value of approximately 4 MHz. Notably, the experimentally measured phonon spectrum indicates vibrational frequencies in the range of 0–4 MHz (as reported in Fig. 5 of this reference). This agreement in the order of magnitude and frequency range shows consistency between the present analytical predictions and experimentally observed microtubule vibrational behavior, thereby providing additional support for the validity of the proposed model.

7. Results and discussion

In this section, the intrinsic structural damping behavior of microtubules is thoroughly investigated through the viscoelastic Kelvin–Voigt damping coefficient (retardation time g). In addition, the influence of the surrounding cytosolic viscous medium (by examining both parameters C_d and R_1) on the natural frequencies and damping ratios is comprehensively analyzed. Furthermore, other influential factors, such as the nonlocal parameter, the material length-scale parameter, various beam theories, and multiple N_S microtubule configurations, are systematically examined to provide a holistic understanding of their combined effects on the dynamic response of microtubules. for this purpose, the following numerical values - all of which are based on experimental and laboratory research documentation [30] - are used to properly obtain numerical results.

$$\rho^s = 2.19\times10^{-7}\ kg/m^2,\ E_x = 1.1\ Gpa,\ E_\theta = 0.01\ Gpa,\ G_{x\theta} = 1.5\ Gpa,\ \upsilon_x = 0.3,\ E_c = 2.5\ Kpa,$$

7.1. Effects of Kelvin–Voigt Viscoelastic Damping Coefficient (Retardation Time)

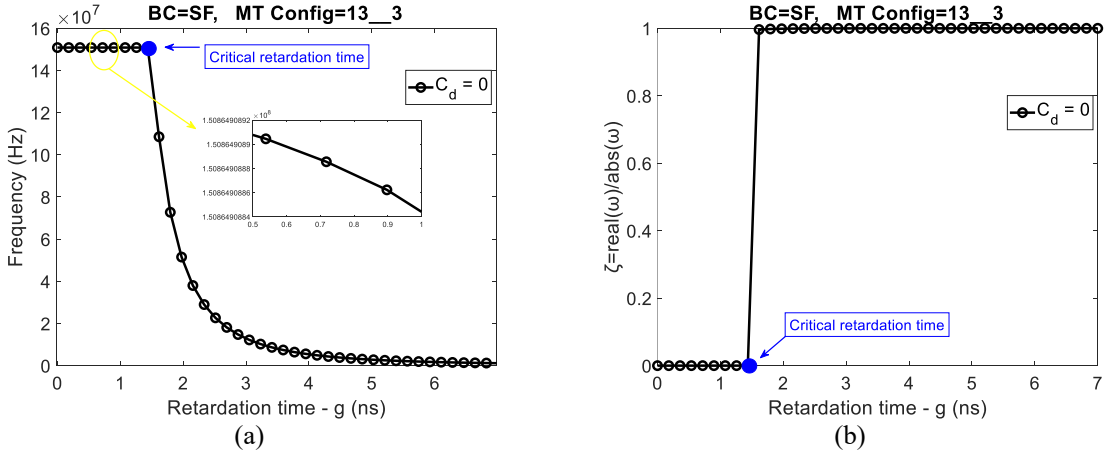

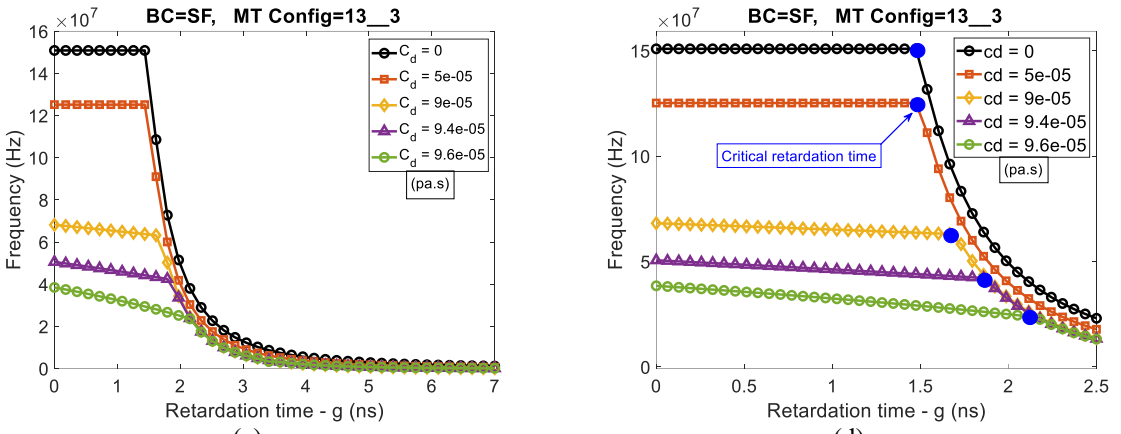

Fig 3: Damping effects of Kelvin–Voigt viscoelastic coefficient (Retardation Time). Common parameters: MT Config=13_3, L=1250 nm, BC=SF, theory=EBT, mode=1. (a) Influence of the MT retardation time on the fundamental frequency. (b) Influence of the retardation time on the damping ratio. (c, d) Influence of the MT retardation time for different values of the damping coefficient of cytosol viscous fluid.

In this study, two distinct damping mechanisms are considered. The first accounts for the structural viscoelastic behavior of microtubules, modeled using the Kelvin–Voigt theory, while the second arises from the intrinsic damping of the surrounding cytosolic viscous fluid, modeled based on the Navier–Stokes equations and the definition of viscous fluid stress. Both effects are examined in the results section.

The most effective way to investigate the role of damping on the vibrational response and stability of the system is to evaluate its influence on the natural frequencies $\mathrm{Im}(\hat{\omega})$ (imaginary part of the complex frequency) together with its effect on the real part of the complex frequency $\mathrm{Re}(\hat{\omega})$, often referred to as the damping frequency.

Error! Reference source not found.(a) illustrates the effect of the structural viscoelastic damping coefficient of the Kelvin–Voigt model (i.e., the retardation time) on the fundamental frequency of the microtubule (the first vibration mode). As expected, the natural frequencies decrease with increasing retardation time, and this trend continues up to approximately g = 1.5 ns.

As shown in **Error! Reference source not found.**(a), before reaching approximately 1.5 seconds of retardation time, the natural frequencies decrease gradually with increasing retardation time, a typical behavior observed in vibrating systems as damping increases. Beyond this point, upon reaching a "critical retardation time" (indicated by the blue point), the vibration frequencies abruptly collapse and approach zero, indicating that the system loses its vibrational behavior and indicating a stronger damping influence on the system's dynamic response.

This phenomenon is more clearly reflected in **Error! Reference source not found.**(b), where the damping ratio $\zeta = \dfrac{|\mathrm{Re}(\hat{\omega})|}{|\hat{\omega}|}$ rises sharply beyond a retardation time of about 1.5 (ns), ultimately reaching unity. This value corresponds exactly to the point "critical retardation time" in **Error! Reference source not found.**(a) where the natural frequencies collapse to zero and the system transitions to non-oscillatory.

Error! Reference source not found.(c) illustrates the effect of the Kelvin–Voigt viscoelastic damping coefficient (retardation time) on the natural frequencies of the system for different values of the cytosolic viscous fluid damping coefficient. As expected, increasing either parameter leads to greater overall damping, which in turn reduces the natural frequencies. In fact, a similar behavior for different values of the foundation damping coefficient is observed. An increase in this secondary damping parameter further reduces the natural frequencies. Such consistent and physically reasonable results confirm the accuracy of the governing equations derived, their implementation, and the overall solution procedure.

To provide greater clarification of the details presented in **Error! Reference source not found.**(c), and to allow a clearer separation and comparison of the individual curves, the same graph is replotted over a smaller range of g in **Error! Reference source not found.**(d). In fact, **Error! Reference source not found.**(d) represents a magnified (zoomed-in) view of **Error! Reference source not found.**(c). A noteworthy observation that becomes more evident in the **Error! Reference source not found.**(d) is that the blue points, representing the critical retardation time, are located on different curves corresponding to different values of the foundation damping coefficient. As shown, with increasing foundation damping coefficient, the critical retardation time is postponed; that is, the system transitions to the non-oscillatory state at higher values of g. In other words, the stability of the system is enhanced.

Another noteworthy point is that the system exhibits its distinct and physically consistent dynamic behaviors within the range of retardation times on the order of nanoseconds (around 1 ns). This observation aligns well with the reported values of retardation time summarized in Section **Error! Reference source not found.**, which were obtained through various experimental and analytical approaches in previous studies. This agreement further confirms both the validity of the estimated retardation time for microtubules and the accuracy of the adopted parameters and solution methodology.

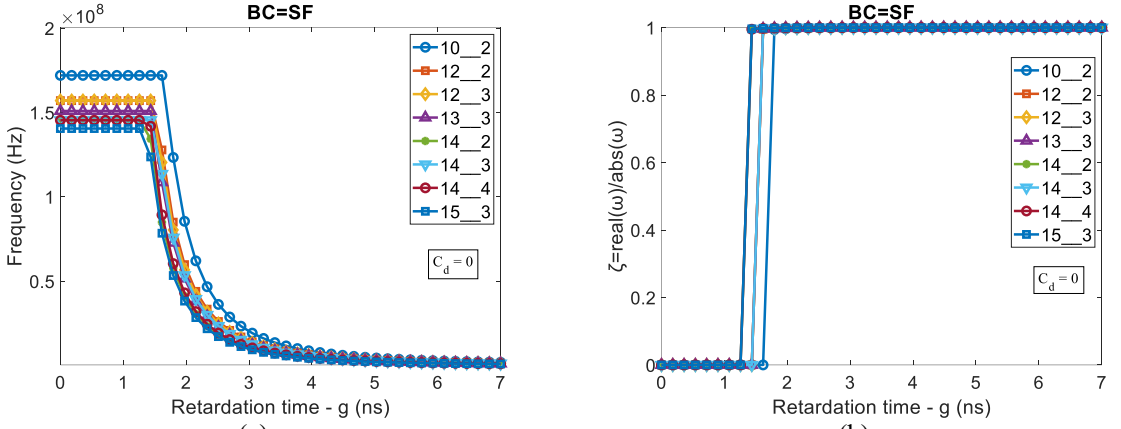

(a) (b)

Fig. 1. Damping effects of Kelvin–Voigt viscoelastic coefficient (Retardation Time). Common parameters: L=1250 nm, BC=SF, theory=EBT, mode=1. (a) Effect of the retardation time for different MT configs. (b) Effect of the retardation time on the damping ratio for different MT configs.

Examining the effects of different N_S microtubule configurations while analyzing the retardation time parameter can provide valuable insights, this aspect is addressed in Fig. 1(a) and Fig. 1(b). In these figures, only the influence of the retardation time damping parameter is considered, while the viscous cytosol damping coefficient is neglected ($C_d = 0$). The observed trends in both the natural frequencies and damping ratios closely resemble those presented in **Error! Reference source not found.**(a) and **Error! Reference source not found.**(b). It is evident that smaller microtubules, such as configuration 10_2, exhibit higher natural frequencies compared to larger ones, an expected and physically consistent outcome.

Another noteworthy observation is that the critical retardation time marking the onset of a sharp decline toward lower natural frequencies, eventually leading to non-oscillatory behavior, slightly differs among various configurations. Specifically, smaller microtubules experience this critical point at a slightly higher (later) retardation time, whereas larger microtubules reach it earlier (at lower g), a pattern clearly visible in Fig. 1(a).

7.2. Damping Effects of Cytosol Viscous Fluid

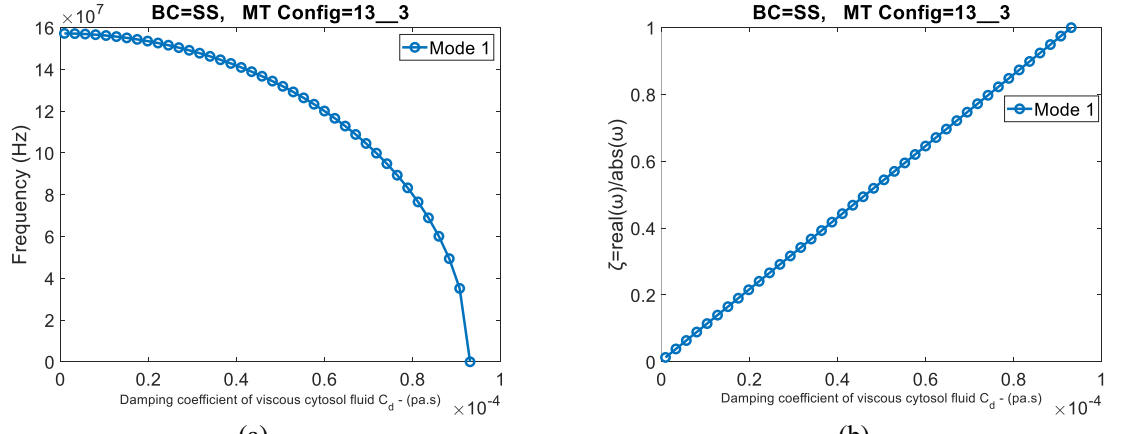

(a) (b)

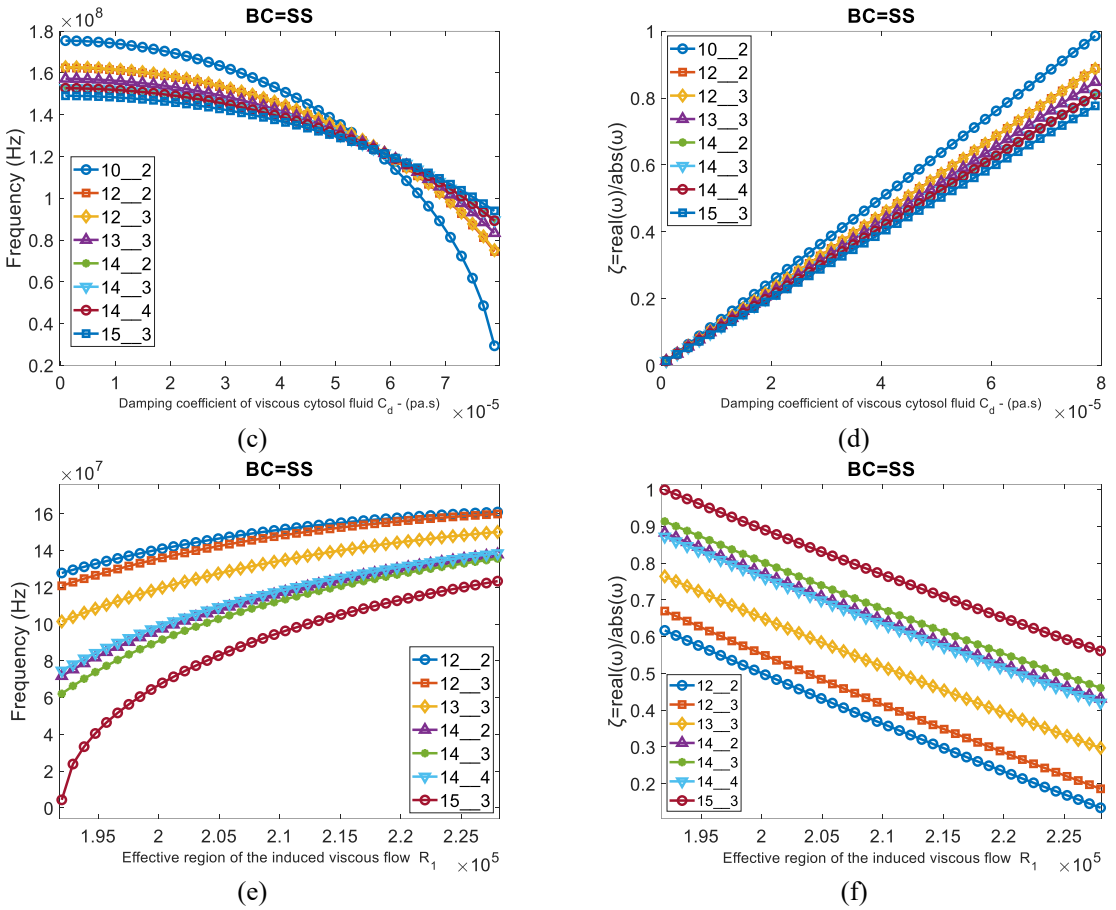

Fig. 2. Damping effects of cytosol viscous fluid. Common parameters: MT Config=13_3 (for Fig. 2(a, b)), L=1250 nm, BC=SS, theory=EBT, mode=1, g=1. (a) Influence on the fundamental frequency (b) Influence on the damping ratio (c) Influence on the fundamental frequency for different MT configs (d) Influence on the damping ratio for different MT configs. Influence of the effective region of the induced viscous flow acting on the microtubule R_1 (e) on the fundamental frequency for different MT configs and (f) on the damping ratio for different MT configs.

A similar behavior to what described in the previous section for structural damping of retardation time is also observed for the cytosolic viscous fluid damping coefficient in Fig. 2(a) and Fig. 2(b). As shown in Fig. 2(a), increasing this coefficient reduces the natural frequencies until they eventually vanish. Correspondingly, Fig. 2(b) illustrates the increase in the damping ratio, starting from $\zeta \approx 0$ (undamped free vibration), followed by a gradual transition within $0 < \zeta < 1$ corresponding to damped oscillations (the underdamped vibration range), and finally, as the damping ratio approaches unity ($\zeta = 1$), the oscillations are effectively suppressed and the motion becomes non-oscillatory.

Although both damping mechanisms (structural viscoelastic MT and cytosolic viscous fluid) exhibit the same overall trend (reducing natural frequencies and driving the system toward non-oscillation), the nature of the transition differs. In the case of retardation time, instability occurs abruptly at a critical value, whereas for the cytosolic viscous fluid damping, the transition develops gradually.

Fig. 2(c) and Fig. 2(d) illustrate this phenomenon more clearly by tracking it across different microtubule configurations.Variations in microtubule configurations generally lead to changes in their inner and outer radii (r_i and r_o) which will consequently be accompanied by a change in mass density as well. As expected, microtubules with smaller diameters or thinner walls (N_S configurations such as 10_2), exhibit higher natural frequencies compared to larger ones (such as configuration 15_3). In other words, as the mean radius or cross-sectional size increases, the natural frequencies tend to decrease. This trend, clearly visible in Fig. 2(c), provides further validation of the governing equations and their implementation.

A noteworthy observation in Fig. 2(c) is that as the damping coefficient of the cytosolic viscous fluid increases, this trend reverses beyond a certain point, smaller microtubules then exhibit lower natural frequencies than larger ones. This inversion arises from the combined influence of geometry and mass variation across different

configurations, which collectively alters the dynamic response of the system. Meanwhile, as shown in Fig. 2(d), microtubules with smaller sizes experience higher damping ratios.

To investigate the effects of cytosolic viscous damping more precisely, it is useful to analyze the influence of the radial distance R_1, which represents the effective region of the induced viscous flow acting on the microtubule. This aspect is examined in Fig. 2(e) and Fig. 2(f). As shown in Fig. 2(e), an increase in the effective range of the viscous fluid leads to higher natural frequencies for all microtubule configurations. This behavior is consistent with Eqs. (20) and (21), since enlarging the effective radius of the surrounding viscous fluid reduces the overall damping coefficient, thereby increasing the frequencies.

Hence, this analysis provides a more refined assessment of viscous damping effects, as it accounts not only for configuration-dependent variations in mass and geometry but also for the distinct damping force corresponding to each microtubule configuration, computed individually.

7.3. Effect of different theories

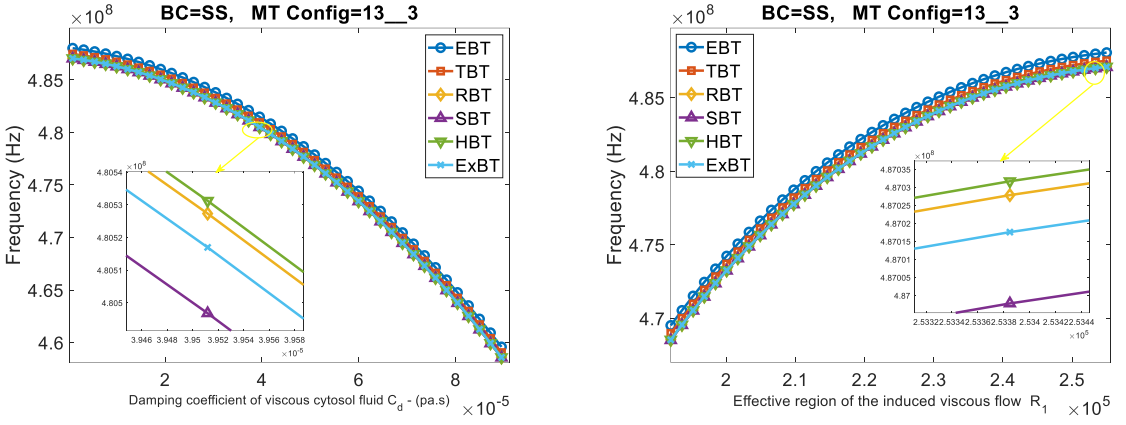

Fig. 3. Effect of different theories on natural frequencies of microtubules. Common parameters: MT Config=13_3, L=1250 nm, BC=SS, mode=4, g=0.26 ns. (a) Influence of damping coefficient of cytosol viscous fluid, C_d. (b) Influence of the effective region of the induced viscous flow acting on the microtubule R_1.

Fig. 3 illustrates the influence of different beam theories on the natural frequencies of microtubule vibrations for various values of the cytosol viscous fluid damping coefficient. Fig. 3(a) presents the fourth vibration mode (chosen for clearer distinction) obtained using the classical and higher-order beam theories (HOBT). Only minor discrepancies are observed, confirming the correctness of the governing equations and their implementation. As also noted in previous studies [12], the Euler–Bernoulli theory slightly overestimates the frequencies because it neglects transverse shear deformation. The close agreement and consistent ranking among the theories further validate the proposed solution approach.

The natural frequencies decrease with increasing cytosolic viscous damping (which enhances the overall damping of the system), a result that is physically reasonable and consistent with fundamental mechanical principles.

Fig. 3(b) shows the same trend when the radial distance (R_1) of the effective region of the induced viscous flow acting on the microtubule is varied. According to Eqs. (20) and (21), increasing R_1 reduces the effective viscous damping coefficient; thus, an inverse relationship compared to Fig. 3(a) is observed, providing additional confirmation of the model's validity. As expected, the Euler–Bernoulli theory yields the highest frequencies, followed by the Timoshenko model, while the HOBT predict slightly lower values.

7.4. Effects of NSGT parameters:

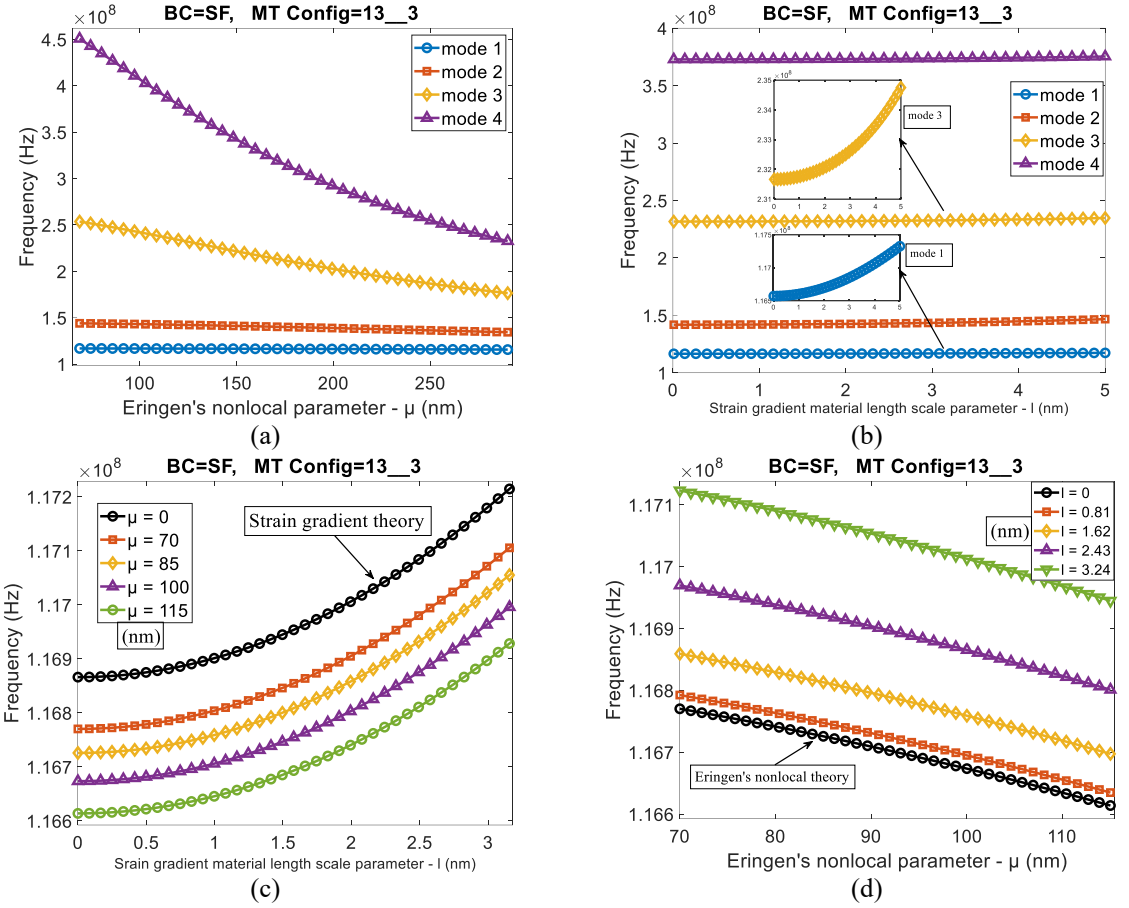

Fig. 4. Natural frequencies of microtubules under NSGT theory. Common parameters: MT Config=13_3, L=1250 nm, BC=SF, theory=RBT, mode=1(except Fig. 4(c, d)). (a) Effect of Eringen nonlocal parameter ($l = 1.25\,nm$); (b) Effect of strain gradient parameter ($\mu = 125\,nm$); (c) Effect of strain gradient parameter at different nonlocal parameters; (d) Effect of nonlocal parameter at different strain gradient parameters

As shown in Fig. 4(a), increasing the Eringen's nonlocal parameter μ leads to a reduction in the natural frequencies of microtubule vibrations across all modes, which is consistent with similar studies [26]. However, this effect becomes more pronounced in higher vibration modes. Moreover, the influence of the material length scale parameter l associated with the strain gradient theory can be observed in Fig. 4(b). An increase in this parameter results in higher natural frequencies for all vibration modes, although the magnitude of these changes is relatively gentel, especially when compared to the effects of the Eringen's nonlocal parameter.

Fig. 4(c) and Fig. 4(d) provide a more detailed investigation of the simultaneous effects of the NSGT parameters. In Fig. 4(c), the influence of the strain gradient parameter l on the natural frequencies is illustrated for different values of the nonlocal parameter, along with the curve corresponding to $\mu = 0$ (pure strain gradient theory), which is shown in black. Similarly, Fig. 4(d) presents the effect of the nonlocal parameter μ on the natural frequencies for various values of the strain gradient parameter. In this case, the curve corresponding to $l = 0$ (pure Eringen's nonlocal theory) is also depicted in black.

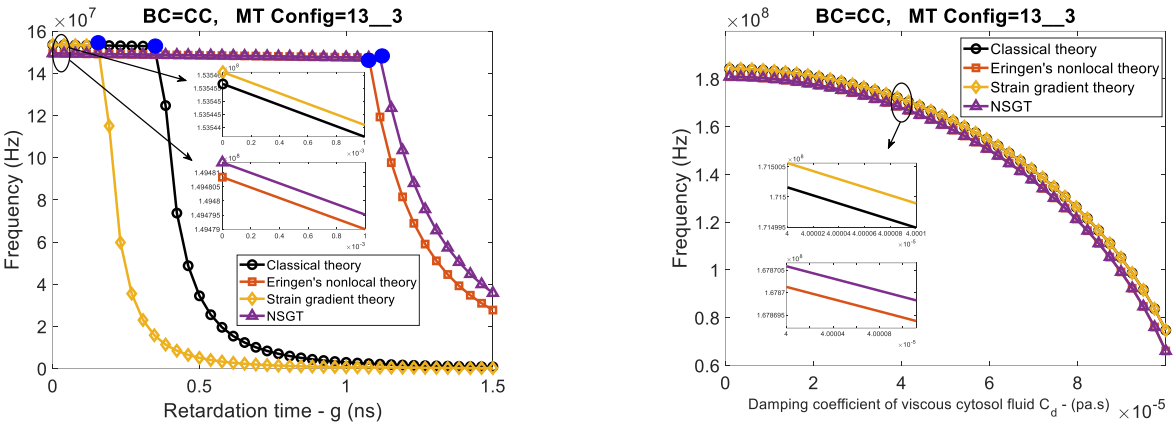

Fig. 5. Effect of small-scale theories. Common parameters: MT Config=13_3, BC=CC, theory=EBT, mode=1. (a) Effect of retardation time; (b) Effect of viscous cytosol damping coefficient.

To provide a clearer and more in-depth understanding of the interaction and influence of nonlocal parameters and damping on the system, Fig. 5(a, b) are presented. Fig. 5(a) illustrates the natural frequencies of the microtubule as a function of the retardation time. What makes this figure particularly valuable and distinctive is that it has been plotted for various small-scale theories, including Eringen's Nonlocal Theory, the Strain Gradient Theory, the Nonlocal Strain Gradient Theory, as well as the Classical Theory (without considering small-scale effects).

It is observed that the overall trend of the curves follows the same pattern as in **Error! Reference source not found.**. However, differences among the various small-scale theories are evident. One notable point is that the natural frequencies in the oscillatory region (i.e., before reaching the critical retardation time) are very close for all four theories, although slight differences exist. The highest natural frequency corresponds to the Strain Gradient Theory. This result is logically expected, since, as shown in Fig. 4(b), the presence or increase of the material length-scale parameter in the Strain Gradient Theory leads to an increase in the natural frequencies. This behavior is consistently observed here as well.

The Classical Theory (without considering small-scale effects) ranks second. It is further observed that the lowest natural frequencies correspond to Eringen's Nonlocal Theory. This is also consistent with Fig. 4(a), where the presence or increase of the nonlocal parameter reduces the natural frequencies of the system. The Nonlocal Strain Gradient Theory occupies the third position. This is because the nonlocal parameter tends to decrease the natural frequencies, whereas the material length-scale parameter tends to increase them; consequently, their effects partially counterbalance each other.

In contrast to the oscillatory region of Fig. 5(a), where the differences among the theories are relatively small, another significant aspect of this figure is that the critical retardation time differs markedly among the various small-scale theories. Specifically, the smallest critical retardation time corresponds to the Strain Gradient Theory, followed by the Classical Theory in second place, Eringen's Nonlocal Theory in third place, and finally the Nonlocal Strain Gradient Theory exhibiting the largest critical retardation time.

The considerable differences between the latter two theories (particularly the |Nonlocal Strain Gradient Theory) and the first two (the Classical and Strain Gradient Theories) clearly show how the selection of an appropriate small-scale theory can significantly influence the accuracy of the results and the prediction of system stability.

In Fig. 5(b), a similar investigation is carried out, this time with respect to variations in the damping coefficient of the cytosol viscous fluid. It is observed that the overall trend is consistent with Fig. 2(a), where an increase in the medium damping (i.e., the surrounding medium of the microtubule) gradually reduces the natural frequencies of the system for all considered small-scale theories. In this case, no significant difference is observed among the different small-scale theories. Rather, the Strain Gradient and Classical Theories follow very similar trends and remain close to each other, while the Nonlocal Strain Gradient Theory and Eringen's Nonlocal Theory likewise exhibit very close behavior along this path.

7.5. Effect of microtubule length

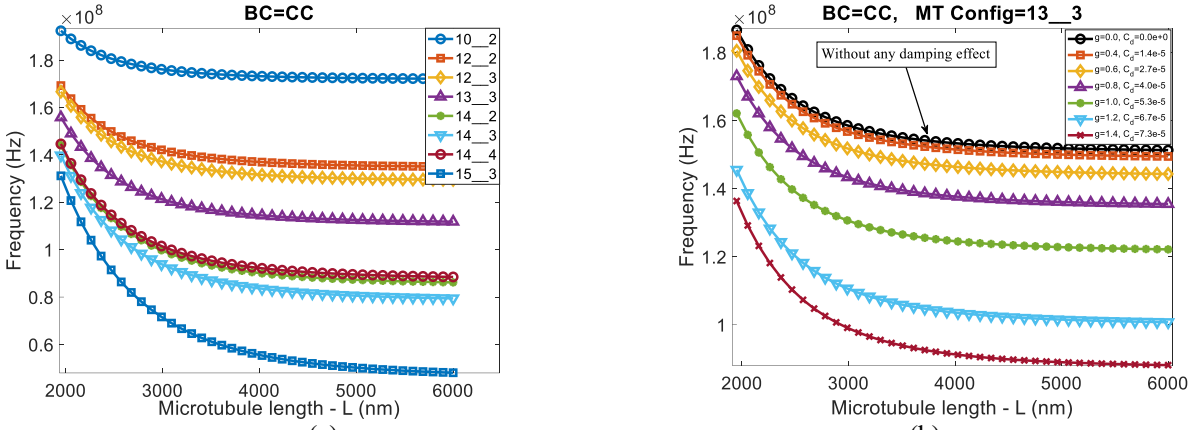

Fig. 6. Effect of microtubule length. Common parameters: MT Config=13_3 (Fig. 6(b)), BC=CC, theory=EBT, mode=2, g=0.26 (Fig. 6(a)). (a) for different MT configs; (b) for different combinations of Retardation time and viscous cytosol damping coefficient.

Since microtubules within cells exist in a wide range of lengths, examining the effects of this parameter is of great importance and practical relevance. This becomes particularly significant when such an investigation is combined with the study of different microtubule N_S configurations, that are also naturally observed in cells. Fig. 6(a) presents such an analysis on the natural vibration frequencies of microtubules. As can be seen, and as expected, increasing the microtubule length leads to a decrease in their natural frequencies. However, this effect occurs with varying intensity and magnitude depending on the configuration. Specifically, microtubules with smaller configurations, such as 10_2, exhibit higher vibration frequencies compared to those with larger configurations like 15_3. Another notable observation is that the reduction in frequency due to increasing length is less pronounced in smaller configurations, whereas microtubules with larger configurations are more sensitive to changes in length.

Fig. 6(b) again examines the influence of length on the vibration frequencies of microtubules, but this time for various combinations of two damping parameters: the retardation time and the viscous damping coefficient of the cytosolic fluid. As expected, the results show that (i) increasing the microtubule length consistently reduces its natural frequencies, and (ii) increasing either damping parameter ultimately decreases the natural frequencies. This consistent trend confirms the correctness of the derived equations, their implementation, and the obtained numerical results. One of the curves in Fig. 6(b) also corresponds to the undamped case, which exhibits the highest frequencies among all the examined conditions.

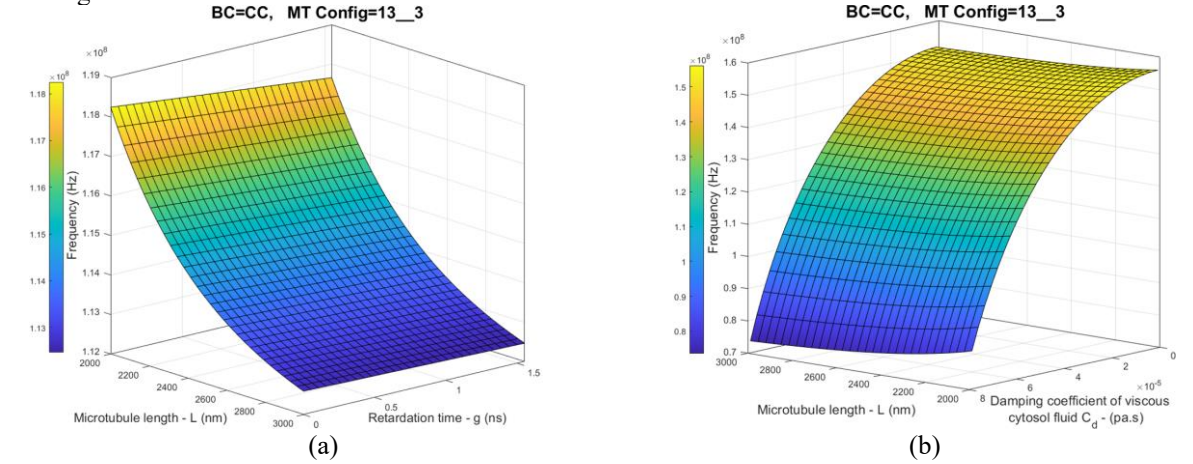

Fig. 7. Combined effects of MT length and damping. Common parameters: MT Config=13_3, BC=CC, theory=EBT, mode=1. (a) Effect of retardation time; (b) Effect of viscous cytosol damping coefficient.

To further clarify the combined effects of microtubule length variation and system damping (including both the structural damping of the microtubule and the viscous damping of the surrounding cytosol fluid), three-dimensional plots are presented in Fig. 7(a, b).

Fig. 7(a) illustrates the simultaneous influence of microtubule length and the structural damping coefficient (retardation time). The behavior of the natural frequencies with increasing microtubule length follows the expected

physical trend, consistent with Fig. 6; that is, the frequencies decrease with a pronounced slope as the length increases.

At the same time, increasing the retardation time also leads to a reduction in the natural frequencies. However, this decrease occurs with a considerably milder slope compared to the effect of length variation observed in Fig. 7(a). This observation highlights the extent to which the structural damping of the microtubule can influence the system's natural frequencies.

On the other hand, Fig. 7(b) simultaneously depicts the effects of microtubule length variation and changes in the viscous damping coefficient of the cytosol fluid. Here as well, increasing either the length or the viscous damping coefficient results in a decrease in the natural frequencies, confirming the physical consistency of the results.

However, if attention is focused solely on the effect of length variation in both figures, an important distinction emerges. In Fig. 7(a), the reduction in frequencies due to increasing microtubule length is sharp and clearly pronounced. In contrast, in Fig. 7(b), the same length-induced reduction appears more gradual and limited. This is because the substantial changes in frequency caused by variations in the viscous damping coefficient overshadow the influence of length, even though the range of microtubule length (2000–3000 nm) is identical in both figures.

In this sense, the microtubule length plays a comparative role between the two figures, allowing a clearer understanding of the relative magnitude of the two damping mechanisms.

From the comparison of these two figures, it can be concluded that both structural damping of the microtubule and viscous damping of the surrounding cytosol fluid reduce the natural frequencies, which is an expected and physically reasonable result. Nevertheless, the effect of the viscous damping coefficient of the cytosol fluid is significantly more pronounced than the corresponding effect of the structural damping (retardation time) of the microtubule.

8. Conclusion

In this study, for the first time, a detailed investigation was conducted on the damping properties of microtubules (MTs) and their surrounding environment. The intrinsic viscoelastic behavior of MTs was modeled through the Kelvin–Voigt framework, coupled with a proper viscoelastic foundation model that accounts for the viscous damping of the cytosolic fluid, forming a comprehensive viscoelastic representation. Moreover, various N–S configurations of microtubules, which naturally exist in cells, were considered for the first time within a vibration–mechanical analysis

The proposed model incorporates the orthotropic nature of MTs, surface elasticity theory, and the nonlocal strain gradient theory (NSGT) to accurately capture size-dependent responses and to evaluate their effects on natural frequencies and damping ratios. The governing equations were formulated using Hamilton's principle and solved numerically—along with the corresponding boundary conditions—by the differential quadrature (DQ) method to achieve high computational accuracy. Systematic parametric studies were performed to explore the effects of key parameters, including retardation time, cytosolic fluid damping, nonlocal parameter, material length-scale parameter, MT length, beam theory, and different N_S configurations.

The results reveal that although an increase in both structural viscoelastic damping of the MT and viscous damping of the cytosolic fluid reduces the natural frequencies and drives the system toward a non-oscillatory state, the transition mechanisms differ. In the case of retardation time, an abrupt reduction occurs beyond a critical value, while for the cytosolic viscous damping, the transition develops gradually. One of the key findings of this work is the identification of this critical retardation time, beyond which the decrease in natural frequencies intensifies sharply, and the system shifts to a non-oscillatory regime. After this point, the damping ratio rapidly increases and eventually approaches unity.

It was also observed that smaller microtubules, such as the 10_2 configuration, exhibit higher natural frequencies compared to larger ones. Furthermore, increasing the MT length consistently decreases its natural frequencies, with larger configurations showing higher sensitivity to length variations. Notably, microtubules with larger configurations also reach the critical retardation time earlier (at lower values of g).

Another important observation is that the system exhibits distinct and physically consistent dynamic behaviors within the range of retardation times on the "nanosecond order" (approximately 1 ns). This agrees well with previously reported retardation times summarized in Section **Error! Reference source not found.**, obtained through various experimental and analytical approaches. **This finding** is particularly valuable for future research, as it independently confirms, through a vibrational analysis approach, the same order of magnitude (around or below 1 nanosecond) for the microtubule retardation time that has been estimated using other experimental and theoretical methods reported in the literature.

Appendix

Table 4: Classical and non-classical stress resultants

The classical stress resultants

$$\{N,M,M_n,Q\}^{cl}=\int_A\begin{Bmatrix}\sigma_{xx}\\ \sigma_{xx}z\\ \sigma_{xx}f(z)\\ \tau_{xz}\dfrac{\mathrm{d}}{\mathrm{d}z}f(z)\end{Bmatrix}dA+\sum_{i=1}^{2}\oint_{\Gamma_i}\begin{Bmatrix}\sigma_{xx}^{s}\\ \sigma_{xx}^{s}z\\ \sigma_{xx}^{s}f(z)\\ \tau_{xz}^{s}\dfrac{df(z)}{dz}\end{Bmatrix}ds \tag{41}$$

The non-classical stress resultants

$$\{N,M,M_n,Q\}^{ncl}=\int_A\begin{Bmatrix}t_{xx}\\ t_{xx}z\\ t_{xx}f(z)\\ t_{xz}\dfrac{\mathrm{d}}{\mathrm{d}z}f(z)\end{Bmatrix}dA \tag{42}$$

Here, A denotes the domain of integration over the cross-section of the MT, while Γ_1 and Γ_2 represent the domains of integration along the outer and inner boundaries of the MT cross-section, respectively

Classical governing equations:

$$\delta u:-\rho A\left(\frac{\partial^2}{\partial t^2}u(x,t)\right)+\frac{\partial}{\partial x}N(x,t)=0 \tag{43}$$

$$\begin{aligned}&\delta w:-2\rho I_3\left(\frac{\partial^4}{\partial x^2\partial t^2}w(x,t)\right)+\rho I_3\left(\frac{\partial^3}{\partial x\partial t^2}\varphi(x,t)\right)+\rho I_1\left(\frac{\partial^4}{\partial x^2\partial t^2}w(x,t)\right)\\&+\rho I_4\left(\frac{\partial^4}{\partial x^2\partial t^2}w(x,t)\right)-\rho I_4\left(\frac{\partial^3}{\partial x\partial t^2}\varphi(x,t)\right)\\&-\rho A\left(\frac{\partial^2}{\partial t^2}w(x,t)\right)+\frac{\partial^2}{\partial x^2}M(x,t)-\frac{\partial^2}{\partial x^2}M_n(x,t)\\&+\frac{\partial}{\partial x}Q(x,t)-k_w w(x,t)+k_g\left(\frac{\partial^2}{\partial x^2}w(x,t)\right)-C_d\left(\frac{\partial}{\partial t}w(x,t)\right)=0\end{aligned} \tag{44}$$

$$\begin{aligned}&\delta\varphi:-\rho I_3\left(\frac{\partial^3}{\partial x\partial t^2}w(x,t)\right)+\rho I_4\left(\frac{\partial^3}{\partial x\partial t^2}w(x,t)\right)\\&-\rho I_4\left(\frac{\partial^2}{\partial t^2}\varphi(x,t)\right)-\frac{\partial}{\partial x}M_n(x,t)+Q(x,t)=0\end{aligned} \tag{45}$$

Classical boundary condition equations:

$$\delta u:$$
$$u\big|_0^L = 0 \overset{or}{\longleftrightarrow} -N(x,t)\big|_0^L = 0 \tag{46}$$

$$\delta w:$$
$$w\big|_0^L = 0 \overset{or}{\longleftrightarrow} \tag{47}$$
$$\left.\begin{aligned} &-\rho\left(I_1 + I_4 - 2I_3\right)\left(\frac{\partial^3}{\partial t^2 \partial x}\, w(x,t)\right) - \rho\left(I_3 - I_4\right)\left(\frac{\partial^2}{\partial t^2}\, \varphi(x,t)\right) \\ &-\frac{\partial}{\partial x}\, M(x,t) + \frac{\partial}{\partial x}\, M_n(x,t) - Q(x,t) - \frac{1}{2}k_g\left(\frac{\partial}{\partial x}\, w(x,t)\right) \end{aligned}\right|_0^L = 0$$

$$\delta\varphi:$$
$$\varphi\big|_0^L = 0 \overset{or}{\longleftrightarrow} M_n(x,t)\big|_0^L = 0 \tag{48}$$

$$\frac{\partial}{\partial x}\delta w:$$
$$\frac{\partial w}{\partial x}\bigg|_0^L = 0 \overset{or}{\longleftrightarrow} \tag{49}$$
$$M(x,t) - M_n(x,t) + \frac{1}{2}k_g w(x,t)\bigg|_0^L = 0$$

References

[1] F. Pampaloni, E.-L. Florin, Microtubule architecture: inspiration for novel carbon nanotube-based biomimetic materials, *Trends in biotechnology,* Vol. 26, No. 6, pp. 302-310, 2008.

[2] A. A. Aslam, C. Prodan, Experimentally measured phonon spectrum of microtubules, *Journal of Physics D: Applied Physics,* Vol. 53, No. 2, pp. 025401, 2019.

[3] H.-S. Shen, Nonlinear vibration of microtubules in living cells, *Current Applied Physics,* Vol. 11, No. 3, pp. 812-821, 2011.

[4] Z. J. Donhauser, W. B. Jobs, E. C. Binka, Mechanics of microtubules: effects of protofilament orientation, *Biophysical journal,* Vol. 99, No. 5, pp. 1668-1675, 2010.

[5] D. Chrétien, S. D. Fuller, Microtubules switch occasionally into unfavorable configurations during elongation, *Journal of molecular biology,* Vol. 298, No. 4, pp. 663-676, 2000.

[6] V. Hunyadi, D. Chretien, I. M. Janosi, Mechanical stress induced mechanism of microtubule catastrophes, *Journal of molecular biology,* Vol. 348, No. 4, pp. 927-938, 2005.

[7] P. J. de Pablo, I. A. T. Schaap, F. C. MacKintosh, C. F. Schmidt, Deformation and collapse of microtubules on the nanometer scale, *Physical review letters,* Vol. 91, No. 9, pp. 098101, 2003.

[8] I. A. T. Schaap, C. Carrasco, P. J. de Pablo, F. C. MacKintosh, C. F. Schmidt, Elastic response, buckling, and instability of microtubules under radial indentation, *Biophysical journal,* Vol. 91, No. 4, pp. 1521-1531, 2006.

[9] J. Y. Wu, H. Yuan, L. Y. Li, Mathematical modelling of axonal microtubule bundles under dynamic torsion, *Applied Mathematics and Mechanics,* Vol. 39, No. 6, pp. 829-844, 2018.

[10] M. R. G. Arani, Z. K. Maraghi, E. Haghparast, Dynamic behavior of anisotropic protein microtubules immersed in cytosol via Cooper–Naghdi thick shell theory, *Journal of Solid Mechanics,* Vol. 10, No. 5, pp. 753-765, 2018.

[11] A. G. Arani, A. A. Shirali, M. N. Farahani, S. Amir, A. Loghman, Nonlinear vibration analysis of protein microtubules in cytosol conveying fluid based on nonlocal elasticity theory using differential quadrature method, *Proceedings of the Institution of Mechanical Engineers, Part C: Journal of Mechanical Engineering Science,* Vol. 227, No. 1, pp. 137-145, 2013.

[12] M. Şimşek, J. N. Reddy, Bending and vibration of functionally graded microbeams using a new higher order beam theory and the modified couple stress theory, *International Journal of Engineering Science,* Vol. 64, pp. 37-53, 2013.

[13] H. F. Lodish, A. Berk, C. Kaiser, M. Krieger, A. Bretscher, H. L. Ploegh, K. C. Martin, M. B. Yaffe, A. Amon, 2021, *Molecular cell biology*, WH Freeman New York,

[14] M. A. Juanes, C. P. Fees, G. J. Hoeprich, R. Jaiswal, B. L. Goode, EB1 directly regulates APC-mediated actin nucleation, *Current Biology,* Vol. 30, No. 23, pp. 4763-4772, 2020.

[15] C. Leterrier, The axon initial segment: an updated viewpoint, *Journal of Neuroscience,* Vol. 38, No. 9, pp. 2135-2145, 2018.

[16] T. Li, A mechanics model of microtubule buckling in living cells, *Journal of biomechanics,* Vol. 41, No. 8, pp. 1722-1729, 2008.

[17] A. Farajpour, A. Rastgoo, M. Mohammadi, Surface effects on the mechanical characteristics of microtubule networks in living cells, *Mechanics Research Communications,* Vol. 57, pp. 18-26, 2014.

[18] M. E. Gurtin, A. I. Murdoch, Surface stress in solids, *International journal of Solids and Structures,* Vol. 14, No. 6, pp. 431-440, 1978.

[19] A. G. Arani, M. Abdollahian, M. H. Jalaei, Vibration of bioliquid-filled microtubules embedded in cytoplasm including surface effects using modified couple stress theory, *Journal of theoretical biology,* Vol. 367, pp. 29-38, 2015.

[20] G. R. Cowper, The shear coefficient in Timoshenko's beam theory, *Journal of applied mechanics,* Vol. 33, No. 2, pp. 335-340, 1966.

[21] O. Wagner, J. Zinke, P. Dancker, W. Grill, J. Bereiter-Hahn, Viscoelastic properties of f-actin, microtubules, f-actin/α-actinin, and f-actin/hexokinase determined in microliter volumes with a novel nondestructive method, *Biophysical Journal,* Vol. 76, No. 5, pp. 2784-2796, 1999.

[22] K. R. Foster, J. W. Baish, Viscous damping of vibrations in microtubules, *Journal of Biological Physics,* Vol. 26, No. 4, pp. 255-260, 2000.

[23] J. Pokorný, Viscous effects on polar vibrations in microtubules, *Electromagnetic Biology and Medicine,* Vol. 22, No. 1, pp. 15-29, 2003.

[24] J. Pokorný, Excitation of vibrations in microtubules in living cells, *Bioelectrochemistry,* Vol. 63, No. 1-2, pp. 321-326, 2004.

[25] A. Shamloo, F. Manuchehrfar, H. Rafii-Tabar, A viscoelastic model for axonal microtubule rupture, *Journal of biomechanics,* Vol. 48, No. 7, pp. 1241-1247, 2015.

[26] C. W. Lim, G. Zhang, J. N. Reddy, A higher-order nonlocal elasticity and strain gradient theory and its applications in wave propagation, *Journal of the Mechanics and Physics of Solids,* Vol. 78, pp. 298-313, 2015.

[27] C. Shu, 2012, *Differential quadrature and its application in engineering*, Springer Science & Business Media,

[28] B. Gu, Y. W. Mai, C. Q. Ru, Mechanics of microtubules modeled as orthotropic elastic shells with transverse shearing, *Acta Mechanica,* Vol. 207, No. 3, pp. 195-209, 2009.

[29] O. Civalek, B. Akgoz, Free vibration analysis of microtubules as cytoskeleton components: nonlocal Euler-Bernoulli beam modeling, 2010.

[30] E. Memet, F. Hilitski, M. A. Morris, W. J. Schwenger, Z. Dogic, L. Mahadevan, Microtubules soften due to cross-sectional flattening, *Elife,* Vol. 7, pp. e34695, 2018.